Characterization of UV–Vis–NIR optical constants of encapsulant for accurate determination of absorption and backscattering losses in photovoltaics modules

Julien Eymard, Raphael Clerc, Vincent Duveiller, Benjamin Commault, Mathieu Hebert

Characterization of UV-Vis-NIR optical constants of encapsulant for accurate determination of absorption and backscattering losses in photovoltaics modules

Julien Eymard [1,2], Raphael Clerc[2], Vincent Duveiller[2], Benjamin Commault[1], Mathieu Hebert[2]

1 Univ. Grenoble Alpes, CEA, Liten, INES, 73375 Le Bourget du Lac, France

2 Université de Lyon, UJM-Saint-Etienne, CNRS, Institut d'Optique Graduate School, Laboratoire Hubert Curien, UMR 5516, St-Etienne, France.

Corresponding author : raphael.clerc@institutoptique.fr

Highlights

- Determine optical properties of scattering PV encapsulants is challenging
- A new 4-flux model accounting for anisotropy gives consistent results on TPO
- Position of UV cut-off shows only minor effects on backscattering

Abstract

The determination of the optical properties of encapsulant for photovoltaic modules is essential for cell-to-module (CTM) performance analysis, UV-durability studies and as input parameters of modelling tools. Some innovative polymer encapsulants used in heterojunction module manufacturing, such as polyolefin elastomer or thermoplastic polyolefin, show a non-negligible optical scattering behaviour in addition to refraction and absorption mechanisms, making challenging the extraction of optical properties in general, and optical indices in particular.

In this work, a 4-flux optical model was applied on total and diffuse transmittance and reflectance measurements of a Thermoplastic PolyOlefin (TPO) encapsulant layer to extract values of refractive index, absorption, scattering coefficient and anisotropy coefficient of scattered light. This model was found mandatory to obtain a satisfactory fitting and plausible value of the optical parameters, in opposition to simpler models based on collimated light, or only diffuse light, or isotropic 4-flux model. The model was applied on two diffusive TPO: a low and a high UV cut-off. The absorption was found respectively to be 1.7 % and 3.8 %. Therefore, a new Cell-To-Module source of loss was identified, induced by the backscattered light in the encapsulant bulk, whose value is near 0.8% of the incoming light in both samples.

Keywords :

- PV Module encapsulant
- Light scattering
- Optical indices measurement
- Cell to Module source of loss

1. Introduction

The photovoltaic industry is experiencing a drastic drop in the price per watt-peak of modules caused by, among other things, the ever-increasing efficiency of silicon solar cells and the management of cell-to-module (CTM) power ratio [1], [2]. Many factors influence the CTM on conventional silicon modules [3], especially optical properties of module layers. Reflection losses at the air/glass interface can be reduced by an antireflective coating or the use of textured glass [4], [5]. Parasitic absorbance in glass bulk can be optimized by selecting low iron content glasses [6], [7]. Optical coupling between solar cell metallization and glass, and between backsheet and glass, impacts the optical gain at module level [8]–[10]. This study focuses on the impact of encapsulation materials on the optical efficiency of the module.

These optical properties of encapsulants influence the cell performance in several ways. Firstly, the refractive index n of the encapsulant affects the amount of reflected light at glass-encapsulant and encapsulant-cell interfaces. Secondly, the extinction coefficient k affects the level of absorption in the encapsulant bulk. Determining the optical properties of the encapsulant is a necessary step for performance analysis, UV-durability studies [11], [12] and module modelling using tools such as ISFH Daidalos™ [13], [14], PVLightHouse Sunsolve™ [15], Optos™ matrix formalism [16], and others.

Ethylene vinyl acetate copolymer (EVA) is currently the most used material, representing more than 90% of market share in 2018 [1], thanks to its low price, good adhesion with glass, and good moisture barrier properties. However, it suffers from non-negligible degradation mechanisms [18] due to acetic acid, which can lead to potential induced degradation (PID) and is not well-suited for some specific cell-technology such as Heterojunction with Intrinsic Thin-Layer (HIT) solar cell, or glass-glass module architecture [19]. Thus, other families of polymer are investigated: polyvinyl butyral (PVB), thermoplastic polyolefin (TPO), polyolefin elastomer (POE), and ionomers [4], [20]. Each family has its own optical properties, governed by the nature of the polymer chains, the additive (adhesion promoter, UV absorber), and the degree of crystallinity. It is well known that these materials can scatter light, as well as absorb and reflect it. The lamination process influences the optical properties, which can be used to control the process quality and the level of curing state of historical encapsulants [17].The reduction of the cooling time of the module after lamination, for example via a cooling press, allows a limitation of the phenomenon of light scattering by TPOs [21].

In this context, it appears necessary to be able to characterise spectrally, accurately – and consistently – the refractive index, absorption and scattering coefficients of such encapsulating materials. Optical properties of transparent polymer have been investigated for a long time [22]. However, most of the methods and measurements proposed so far give only partial information. Light absorption is commonly characterized by the encapsulant transmittance, but it is not representative of real losses in module due to light reflections at the air/layer interface. Coarse characterization of scattering is possible by haze measurement, but is generally not a spectrally resolved measurement [23]. Moreover, some studies characterize absorption ignoring the effect of light scattering at short wavelengths [24]–[27], leading to overestimation of absorption and underestimation of the amount of light reaching the cell. The latter is, however, of great importance: for example, the evaluation of the damp-heat aging test impact on optical performances of silicon and EVA encapsulants can be tricky without taking into account scattering by moisture ingress [11].

To address this issue, recent studies applied the 4-flux model to describe the propagation of collimated and diffuse lights [28], [29], but the optical parameters obtained in these works were not spectrally resolved. Oreski *et al*. have used a 4-flux model to determine spectrally-resolved absorption and scattering coefficients of encapsulants, but the refractive index values were not mentioned in their work [30]. Kempe *et al*. has characterized the spectral absorption in eleven encapsulants of different nature (PDMS, POE, EVA, Ionomer..), without differentiation of absorption and scattering [31]. Other methods like photo-thermal deflection spectroscopy has also been used to

accurately determine absorption and scattering coefficients in low-loss polymer optical waveguides, but using previously determined refractive index values [32]. French *et al*. have used ellipsometry and spectroscopy to determine absorption coefficient, refractive index and haze of several polymer for optics of a CPV system, but with a combination of ellipsometry and thick layer spectroscopy, where consistency of the measurements was not investigated [33].

In conclusion, there is still no practical solution to determine spectrally resolved value of refractive index, absorption coefficient and scattering coefficient simultaneously, using one instrument. Moreover, if the optical constants of standard encapsulants like EVA and silicon can be easily found in literature, values for new encapsulants, needed for simulation tools calibration, are not easily available as far as we know. The aim of this work is thus to propose a reliable method to simultaneously determine spectrally resolved values of refractive index, absorption coefficient and scattering coefficient in the UV, visible and NIR spectral range using a spectrophotometer with integrating sphere, as unique, easily accessible instrument.

The paper is organized as follows: the sample preparation, encapsulant lamination and the spectrophotometer measurements of reflectance and transmittance (total and diffuse) are described in section 2. In section 3, the 4-flux method for optical parameter extraction is presented. Then, results obtained by the 4-flux methods and simpler approaches are compared and discussed in section 4. Finally, section 5 presents an application of the 4-flux method on a low UV cut-off and high UV cut-off TPO encapsulant.

2. Experimental methods

In this section, the process of encapsulant lamination is detailed first, before presenting the method used to measure specular and diffuse reflectance and transmittance.

2.1 Sample preparation

Encapsulant samples are laminated using a membrane laminator. The samples are placed between two isolating and non-adhesive ultra-smooth (root mean square roughness around 50nm) PTFE thermoplastic film with high melting point (> 250°C) and covered by two non-textured glass plates of 10 x 10 cm (see Figure 1). The edges of the laminated {glass / PTFE / encapsulant / PTFE / glass} are closed with a strip of ribbon. Hence, the encapsulant does not flow and keeps the same thickness as it would have in a real module. Once laminated, the samples are separated from glass and non-adhesive film and cut into four pieces of 5x5 cm which can fit the spectrophotometer sample compartments. The thickness is recorded at four points around the middle of the sample with an electronic micrometre FOWLER of 1 µm resolution. Thickness measurement is performed after optical measurements, to prevent deterioration of the surface. Samples are kept in an opaque, airtight bag to prevent from photo-oxidation. Handling of samples is done with disposable gloves to prevent surface contamination with organic compounds.

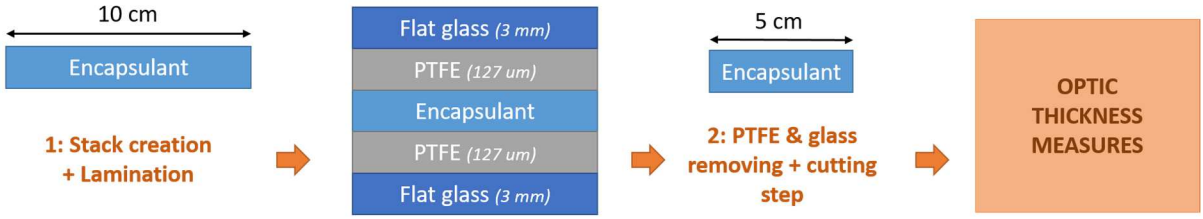

Figure 1: Sample preparation: the encapsulant sheet alone is used for the spectrophotometric measurement.

2.2 Spectral reflectance and transmittance measurements

In this work, a spectrophotometer instrument, allowing specular and diffuse measurements, has been used. It is a high accuracy UV-Vis-NIR PERKINELMER Lambda 950. A deuterium lamp is used for UV measurements between 280 and 320 nm, and a tungsten lamp is used for the remaining wavelengths. The double holographic grating monochromator switches at 860 nm. The beam splitting system for correction of lamp deviation is a chopper wheel with a 46+Hz cycle: dark sample / sample / dark reference / reference and a chopper segment signal correction. The temperature of the room is controlled and ranges from 20.5 to 21.5 °C. The samples are brought into the room one hour before the measurement to ensure a correct thermalization.

The first module – an InGaAs integrating sphere (IS) of 150 mm in diameter – is used for reflectance and transmittance, in total and diffuse modes. It is referred to as "IS 150mm" in the following. The detector is a photomultiplier R6872 for high energy in the whole UV/vis wavelength and a Peltier cooled detector for NIR, the switching occurring at 860 nm. The UV/Vis resolution is less than 0.05 nm and the NIR resolution is less than 0.20 nm. The back aperture for reflectance measurements is a 25 mm diameter hole. The front side aperture for diffuse reflectance measurements is a 30 mm side square. For diffuse transmittance and reflectance measurements, a light trap guarantees a transmittance lower than 0.1 %, eliminating errors due to back reflectance. The diffuse spectralon has been calibrated by LabSphere™. The incident light beam hits the sample with an angle of 8° and every diffuse and collimated rays are collected; the geometry of measurements is thus 8°:d (“d” standing for “diffuse”). The size of the spot is 3 mm wide and 12 mm high.

At the beginning of each series of measurements, a baseline is made to correct any instrument deviation. Measurements are made between 280 nm and 2450 nm with 10 nm steps as recommended by the IEC standard 62788-1-4:2016. The spectralon is systematically placed in the same position, to minimize uncertainty due to its potential inhomogeneity. At the beginning of each series of measurements, a baseline is measured: (i) in transmittance mode, the baseline is a measurement of the transmission without sample to obtain 100% - (ii) in reflectance mode, the baseline is a measurement of the reflectance of the calibrated spectralon. At the end of the measurement serie, baseline is checked for any deviation. A check of the dark level is done after baseline measurement, using a light trap at the back hole of the integrating sphere. It ensures that the spot of the spectrophotometer is correctly aligned with the sample's aperture. The four measurements geometries are illustrated in Figure 2.

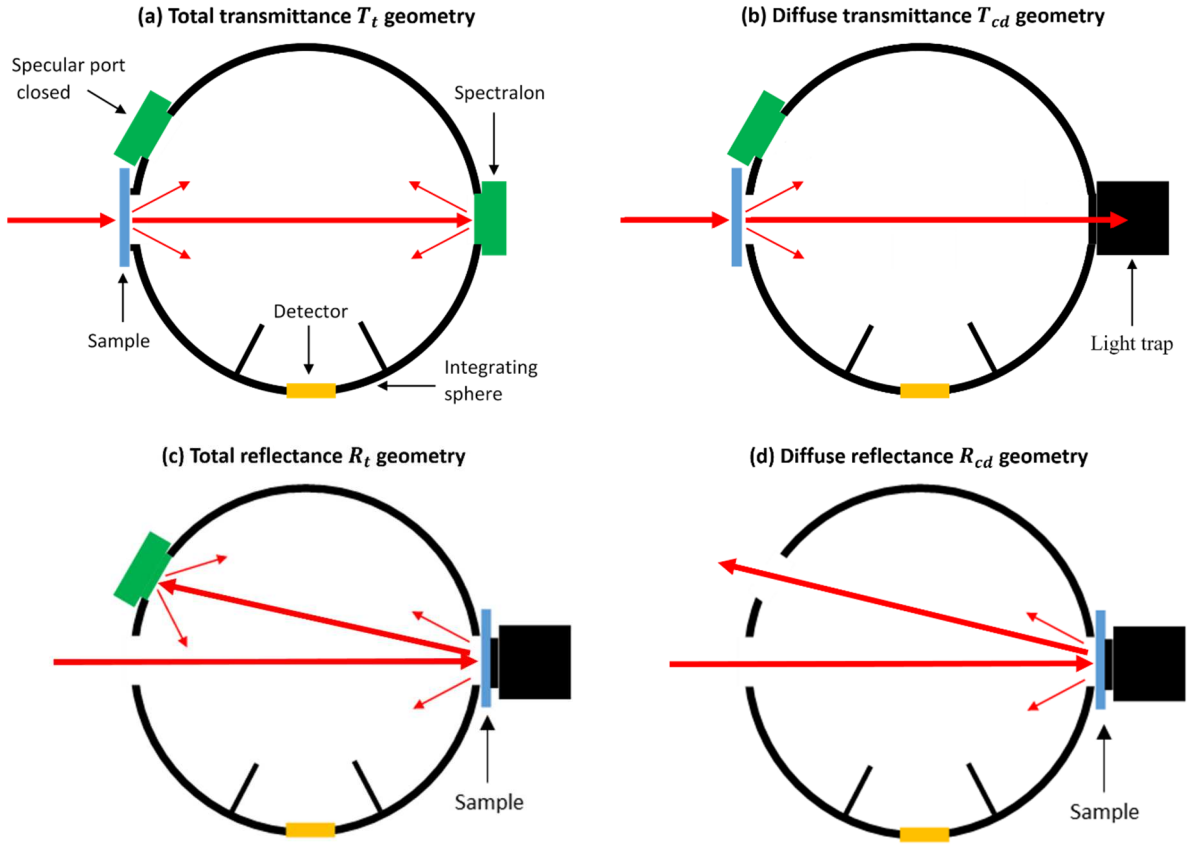

Figure 2: Four measurement geometries used in the work: (a) Total transmittance. (b) Diffuse transmittance. (c) Total reflectance. (d) Diffuse reflectance.

Four physical quantities are measured by the set up:

- First, the total transmittance T_t : in this case, the sample is located at the front port of the integrating sphere and the back port is closed with the LabSphere™ spectralon. Diffuse and collimated rays are measured together.
- Then, the diffuse transmittance T_{cd}: (also denoted as "collimated-to-diffuse" transmittance). In this case, the sample is located at the front port of the integrating sphere and the back port is closed with the light trap. Only diffuse light is measured, since the collimated part leaves the integrating sphere.
- The total reflectance R_t: In this case, the sample is located at the back port of the sphere, the specular light port at 16° from the front port is closed. The light trap is located at the back of the sample. Diffuse and collimated rays are measured together.

- The diffuse reflectance R_{cd}: (also denoted as the “collimated-to-diffuse” reflectance) in this case, the configuration is similar tothe one for measuring the total reflectance, but the specular port is open.

Collimated transmittance T_{cc} and reflectance R_{cc} are computed as $T_{cc} = T_t - T_{cd}$ and $R_{cc} = R_t - R_{cd}$. The size of the specular ports of the integrating sphere to avoid measuring collimated light (for diffuse measurements) is not zero. Consequently, a part of the scattered light may be counted as collimated light. In the current experimental setup, all transmitted rays included in a solid angle of 0.02 sr around the normal are included in the collimated part. All reflected rays included in a solid angle of 0.04 sr around the reflected collimated ray are also counted in the collimated part.

In the next section, a model used to deduce the optical parameters from the reflectance and transmittance measurements is presented.

3. Overview of the optical 4-flux model

In this section, the different procedures used to extract the optical parameters from R and T experiments are reviewed and tested on a reference non diffusing samples (BK7 glass and EVA encapsulants).

3.1 Formalism of the 4-flux model

This section is dedicated to a brief presentation of the 4-flux model by Maheu *et al.* (1984) [34], the starting point of the approach used in this work. It describes the propagation of light through a thick and homogeneous layer, accounting for absorption, reflection and refraction at the interfaces, and scattering (in the Lambertian approximation). Coherence, polarization and non-linearity effects are neglected.

In the case of a layer composed of randomly homogeneously distributed particles, with perpendicular illumination of unpolarised light, the propagation of light in a medium that absorbs and scatters light is governed by the radiative transfer equation [35], [36]:

$$\mu \frac{dI(\tau,\mu)}{d\tau} = -I(\tau,\mu) + \frac{\omega_0}{2}\int_{-1}^{+1} p(\mu,\mu')I(\tau,\mu') - \frac{\omega_0}{4\pi}S(\tau,\mu) \quad (1)$$

where $I(\tau,\mu)$ is the luminance (or specific intensity) of the diffuse radiation at an optical depth τ and the direction of propagation μ. The optical depth is $\tau = (s+a)h$, with s the scaterring coefficient, a the absorbtion coefficient, and h the thickness of the film. The single scattering albedo is defined as $\omega_0 = s/(s+a)$. $p(\mu,\mu')$ is the scattering phase function, i.e., the probability that a scattering event changes the light direction from μ to μ'. Finally, $S(\tau,\mu)$ is the intensity of the collimated beam in the direction μ.

Let define I_d – the forward diffuse flux – and J_d – the backward diffuse flux. The 4-flux model approximates the radiative transport equation, if I_d and J_d are Lambertian. In opposition to the 2-flux model, also known as the Kulbelka-Munk model [37], it also considers the propagation of the collimated (or ballistic) forward flux I_c and collimated outward flux J_c and their coupling with the aforementioned diffused fluxes.

There exist various formulations of the 4-flux model. Maheu *et al.* [34], [38] proposed a four flux model for a scattering layer, accounting for the reflectance and transmittance of its bordering interface. Vargas *et al.*, [39] have generalized the expression of Maheu *et al.*, taking into account different value for forward scattering ratio in up and down direction. The expressions for the diffuse and collimated reflectances are given as functions of light transport parameters *a, s*, ζ, ϵ explained below, and the optical index *n*.

The fraction of irradiance absorbed by a layer of infinitesimal thickness dz is adz, where *a* is the absorption coefficient in m^{-1}. Similarly, the fraction of irradiance scattered by a layer of infinitesimal thickness dz is sdz, where *s* is the scattering coefficient in m^{-1}. The average crossing parameter ϵ is defined as the average path travelled by the diffuse radiation across the layer. If a collimated beam crosses an elementary distance dz, a diffuse radiation travels a distance ϵdz in average. The forward scattering ratio ζ is the ratio of irradiance scattered by the particles in the forward hemisphere divided by the total scattered energy. The ratio of energy back scattered is thus $1-\zeta$. This value is defined for a collimated beam and is considered to be approximatively the same for a diffuse radiation.

According to the previous definitions, the collimated and the diffuse exitance at the surface of an infinite medium without interface with air obey to the coupled balance differential equations (2) to (5):

$$\frac{dI_c}{dz} = (a+s)\,I_c \tag{2}$$

$$\frac{dJ_c}{dz} = -(a+s)J_c \tag{3}$$

$$\frac{dI_d}{dz} = \epsilon(a+(1-\zeta)s)I_d - \epsilon(1-\zeta)sJ_d - \zeta sI_c - (1-\zeta)sJ_c \tag{4}$$

$$\frac{dJ_d}{dz} = \epsilon(1-\zeta)sI_d - \epsilon(a+(1-\zeta)s)J_d + (1-\zeta)sI_c + \zeta sJ_c \tag{5}$$

The reflectance of the interface between the air and the scattering layer are then included in the following form: r_c is the reflectance of the collimated beam, r_d^e is the reflectance of the diffuse radiation flowing inward the layer and r_d^i for the diffuse radiation flowing outward the layer. The reflectance of the collimated beam at normal incidence is expressed as a function of the complex value of the relative refractive index *n* :

$$r_c = |(n-1)/(n+1)|^2 \tag{6}$$

where the symbol $|.|$ denotes the modulus of a complex number. The reflectance r_d of the diffuse radiation, called bi-hemispherical reflectance, is described below in a dedicated section.

The solution of these equations (2-6) requires boundary conditions. In the original model of Maheu *et al*., a reflective background is added behind the sample. The sample and the layer are not in optical contact and are separated by a thick layer of air. The geometry used by Maheu *et al*. is presented in Figure 3. In the present study, as no background is used, its effect is therefore not taken into account in the model presented (the reflectance values of the background are therefore zero and the transmittance values are unity).

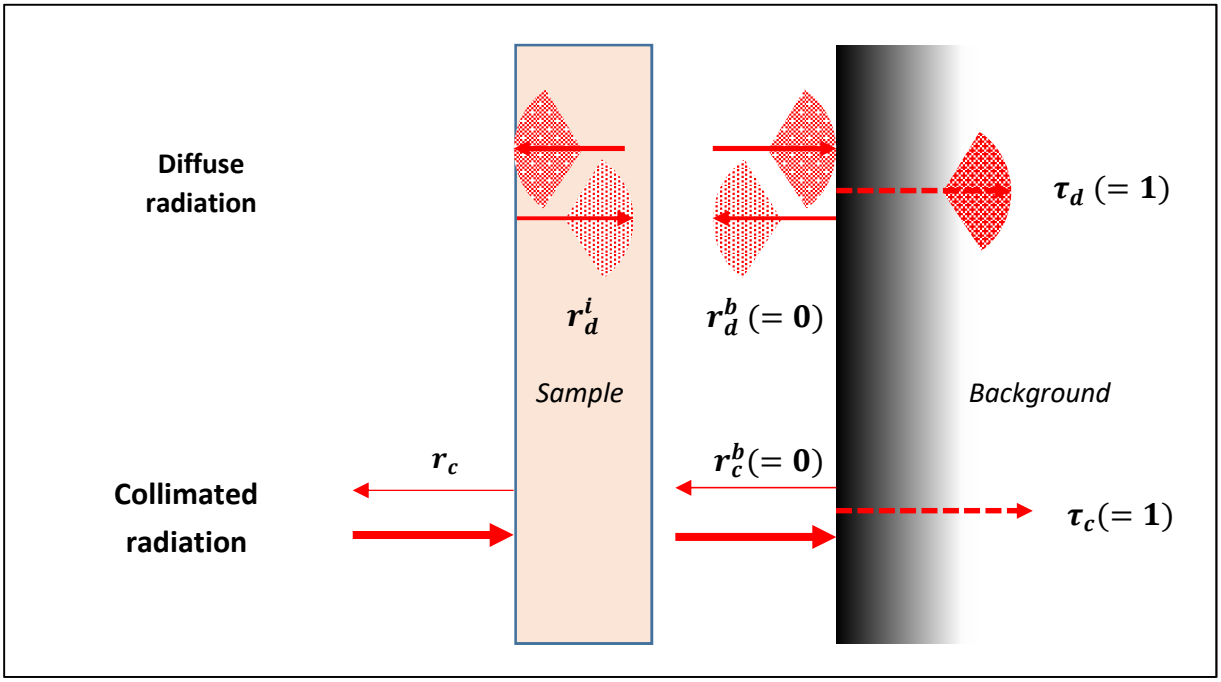

Figure 3: Geometry of the system as studied by Maheu et al. The layer of the sample is placed above a background and separated by a thick layer of air. For directional light at normal incidence, the reflectance of the air/sample interface is r_c, and the one of the air/background is r_c^b. The reflectance of the air/sample interface for a perfectly diffuse light is r_d^i. At the air/background interface the diffuse reflectance is r_d^b. The background has a diffuse transmittance τ_d and a collimated transmittance τ_c. In the geometry of this study, no background is used: in brackets, the corresponding values of reflectance and transmittance are mentioned.

Following Maheu *et al.*, the collimated-to-collimated transmittance T_{cc}, the collimated-to-diffuse transmittance T_{cd}, the collimated-to-collimated reflectance R_{cc}, and the collimated-to-diffuse reflectance R_{cd} are given by:

$$T_{cc} = \frac{(1-r_c)^2 \exp(-(a+s)h)}{-r_c^2 \exp(-2(a+s)h)} \tag{7}$$

$$T_{cd} = \frac{\left(1-r_d^i\right)(1-r_c)\ \exp(-(a+s)h)}{(A_1-(a+s)^2)(1-r_c^2\exp(-2(a+s)h))} \cdot \frac{N_T}{D_T} \tag{8}$$

$$R_{cc} = r_c + \frac{(1-r_c)^2 r_c \exp(-2(a+s)h)}{-r_c^2 \exp(-2(a+s)h)} \tag{9}$$

$$R_{cd} = \frac{\left(1-r_d^i\right)(1-r_c)\exp(-(a+s)h)}{(A_1-(a+s)^2)(1-r_c^2\exp(-2(a+s)h))} \cdot \frac{N_R}{D_R} \tag{10}$$

with:

$$\begin{aligned} N_T = {} & \sqrt{A_1}\left[r_d^i A_3 - A_2 + r_c\left(r_d^i A_2 - A_3\right)\right] ch\left(\sqrt{A_1}h\right) \\ & + \left[\left(A_5 - r_d^i A_4\right)(A_3 + A_2 r_c) - \left(A_4 - r_d^i r_c\right)(A_2 + A_3 r_c)\right] sh\left(\sqrt{A_1}h\right) \\ & + \sqrt{A_1}\left\{\left(A_2 - r_d^i A_3\right)\exp\left((a+s)h\right) + r_c\left(A_3 - r_d^i A_2\right)\exp(-(a+s)h)\right\} \end{aligned} \tag{11}$$

$$D_T = \sqrt{A_1}\left({r_d^i}^2 - 1\right) ch\left(\sqrt{A_1}h\right) + \left[r_d^i\left(A_5 - r_d^i A_4\right) + r_d^i A_5 - A_4\right] sh\left(\sqrt{A_1}h\right) \tag{12}$$

$$\begin{aligned} N_R = {} & (\sqrt{A_1}\left[A_3 + A_2 r_c - r_d^i(A_2 + A_3 r_c)\right] \\ & + \left\{\sqrt{A_1}\left(A_2 r_d^i - A_3\right) ch\left(\sqrt{A_1}h\right)\right. \\ & \left. + \left[A_2\left(A_5 - A_4 r_d^i\right) + A_3\left(A_5 r_d^i - A_4\right)\right] sh\left(\sqrt{A_1}h\right)\right\} \exp\left((a+s)h\right) \\ & + r_c\left\{\sqrt{A_1}\left(A_3 r_d^i - A_2\right) ch\left(\sqrt{A_1}h\right)\right. \\ & \left. + \left[A_3\left(A_5 - A_4 r_d^i\right) + A_2\left(A_5 r_d^i - A_4\right)\right] sh\left(\sqrt{A_1}h\right)\right\} \exp(-(a+s)h) \end{aligned} \tag{13}$$

$$D_R = \sqrt{A_1}\left({r_d^i}^2 - 1\right) ch\left(\sqrt{A_1}h\right) + \left[2A_5 r_d^i - A_4\left(1 + {r_d^i}^2\right)\right] sh\left(\sqrt{A_1}h\right) \tag{14}$$

where the constant A_i are given by:

$$A_1 = \epsilon^2 a[a + 2(1-\zeta)s] \tag{15}$$

$$A_2 = s[\epsilon a\zeta + \epsilon s(1-\zeta) + \zeta(a+s)] \tag{16}$$

$$A_3 = s(1-\zeta)(a+s)(\epsilon - 1) \tag{17}$$

$$A_4 = \epsilon[a + (1-\zeta)s] \tag{18}$$

$$A_5 = \epsilon(1-\zeta)s \tag{19}$$

To summarize, the Maheu *et al.* model allows to calculate four measurable quantities (namely T_{cc}, T_{cd}, R_{cd}, R_{cc}) as functions of five unknown quantities describing the layer optical properties (namely a, s, ϵ, ζ, n), knowing the sample thickness h. Figure 4 summarizes the possible transfers between the incident collimated flux, the reflected fluxes - collimated and diffuse - and the transmitted fluxes - collimated and diffuse

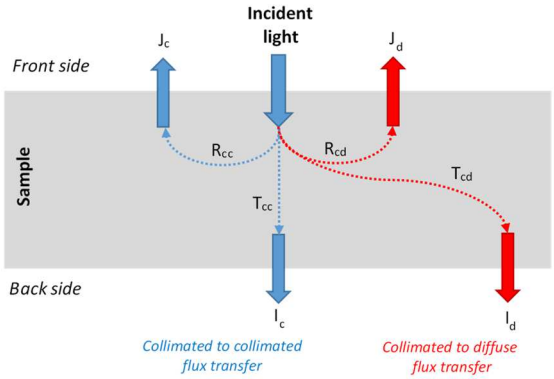

Figure 4: Diagram of the possible transfers between the collimated incident flux and the reflected and transmitted, collimated and diffuse fluxes.

In order to reduce the number of unknown layer optical parameters, Rozé *et al.* [40] have proposed a procedure which allows to express the average crossing parameter ϵ and the forward scattering ratio ζ as functions of the other parameters, and one additional unknown quantity, the asymmetry parameter *g* of the Henyey-Greenstein phase function (see supplementary materials Eq.(1) and Fig. S2). Consequently, the number of unknown optical parameters are now four, namely *a, s, g* and *n*. Examples of average crossing parameters ϵ and forward scattering ratios ζ obtained with this method are given in supplementary materials Fig. S3.

A fitting algorithm is used to solve the system of four equations and four unknowns, by minimising the following objective function "root-mean-square error" $RMSE$ wavelength by wavelength (Equation (20)). The Matlab® function "*fmincon*" has been used, with a sequential quadratic programing algorithm "SQP" described in Nocedal *et al*. [41]. The possibility to fit several samples of the same nature but different thicknesses is added. In this study, to extract the optical parameters of each encapsulant material, we used two samples (*N* = 2) of different thicknesses. The first one is made of a simple sheet of thickness h_1, the second one is made with two sheets for a total thickness $h_2 \approx 2h_1$. (The details of the steps of the optimization routines are given in the supplementary material Fig. S4)

$$RMSE = \sqrt{\frac{\sum_{i=1}^{N}\left(Tcc_n^i - Tcc_e^i\right)^2 + \left(Tcd_n^i - Tcd_e^i\right)^2 + \left(Rcc_n^i - Rcc_e^i\right)^2 + \left(Rcd_n^i - Rcd_e^i\right)^2}{4\,N}} \quad (20)$$

Four experimental measurements T_t, T_{cd}, R_t, R_{cd} are carried out per sample, and the four parameters *a, s, g* and *n* are to be determined. Several reasons led us to use two samples rather than one. First, using more data than necessary increases the reliability of the fitting procedure. Second, it ensures that the optical constants are valid for a range of thicknesses, rather than a single thickness. Finally, if the fit is good for both samples, it is an important indication of volume scattering rather than surface scattering. Indeed, the thicker the sample is, the greater the volume scattering is, which is not obviously the case for surface scattering.

3.2 Improved bi-hemispherical reflectance of the diffuse fluxes at interfaces

The boundary condition requires a value of the bi-hemispherical reflectance r_d^i of the diffuse flux going outward the layer. Assuming that the diffuse fluxes are perfectly Lambertian, the bi-hemispherical reflectance is typically computed by integration of the Fresnel coefficient $R_{i-p/s}$ for polarization p or s over the hemisphere:

$$r_{d-p/s}^{i}(n) = \frac{\int_{\theta=0}^{\frac{\pi}{2}} R_{i-p/s}(\theta, n)\ \sin(2\theta)\, d\theta}{\int_{\theta=0}^{\frac{\pi}{2}} \sin(2\theta)\, d\theta} \tag{21}$$

The total bi-hemispherical reflectance is given by :

$$r_{d}^{i} = \frac{r_{d-p}^{i} + r_{d-s}^{i}}{2} \tag{22}$$

Duntley and Walsh found an analytical solution of this integral, giving the reflectance as a function of the refractive index, as mentioned in equation (23) [42].

$$r_{d}^{i} = \frac{1}{2} + \frac{(n-1)(3n+1)}{6(n+1)^2} + \frac{n^2(n^2-1)^2}{(n^2+1)^3}\ln\left(\frac{n-1}{n+1}\right) - \frac{2n^3(n^2+2n-1)}{(n^2+1)(n^4-1)} + \frac{8n^4(n^4+1)}{(n^2+1)(n^4-1)^2}.\ln(n) \tag{23}$$

However, the assumption of Lambertian diffuse flux is questionable when the considered layers are weakly diffusing (i.e., translucent) or too thin. And even for a highly diffusing layer, the assumption of Lambertian diffuse flux does not hold when scattering is highly anisotropic. Indeed, for a strong anisotropy (g = ±1), the diffuse flux is collimated. In consequence, the reflectance of the interfaces for the the inward and outward fluxes should be equal to the Fresnel reflectance at normal incidence. This issue illustrates one of the limitations of the 4-flux approach in case of anisotropic scattering, anisotropy being included in the bulk equations but not in the boundary conditions. A solving of the radiative transport equation would prevent this issue.

In order to address this issue in an approximated way, we propose to replace the conventional bi-hemispherical reflectance by the following expression, which account for anisotropy:

$$r_{d-p/s}^{i}(n, g) = \frac{\int_{\theta=0}^{\frac{\pi}{2}} R_{i-p/s}(\theta, n)\, P_{HG}(\theta, g) \sin(2\theta)\, d\theta}{\int_{\theta=0}^{\frac{\pi}{2}} P_{HG}(\theta, g) \sin(2\theta)\, d\theta} \tag{24}$$

This new formulation of the bi-hemispherical reflectance accounts for the anisotropy factor *g* and maintains a continuity between the Fresnel reflectance for the collimated case ($g = \pm 1$) and the conventional bi-hemispherical reflectance in the limit case of isotropic diffusion (g = 0). Indeed, the variation of the improved bi-hemispherical reflectance as a function of *g* and *n* is shown in Figure 5, where both reflectances for the flux flowing outward and the flux flowing inward are plotted.

As expected, for a strong anisotropy ($g = \pm 1$), as the diffuse flux is actually directional, the improved bi-hemispherical reflectance of the inward and the outward flux for $n = 1.5$ are the same and coincide with the expected value of 4 % given by the analytical Fresnel reflectance formula. For a perfect isotropy ($g = 0$) and the same value of refractive index *n*, the improved bi-hemispherical reflectance is $r_d^i = 59.6\ \%$, which is the same value as the one yielded by equation (23).

As there is no obvious analytical solution for the improved bi-hemispherical reflectance, its values are all pre-calculated and interpolated by a fifth-degree polynomial as a function of n and g.

However, this approach is not completely accurate. Indeed, when using the equations (24), we only integrate the frontal lobe of the Henyey-Greenstein phase function. This is therefore representative of the forward diffuse flux intercepting the second interface. On the other hand, the backscattered flux in the volume at the first beam pass, which then intercepts the first interface, has an angular distribution given by the back lobe of the phase function. If *g* = 0, the phase function is isotropic, and the problem does not arise. Similarly, if *g* is close to 1, the flux is directional and the backscattered

flux is negligible. On the other hand, for intermediate values of *g*, the angular distributions of the front and back lobes are different, and thus the bi-hemispherical reflectance should be different. This is not the case in the model used: the front and rear interfaces are supposed to be identical. This weakness may result in an error in the extraction of parameters.

First guess of optimization routine, boundaries of the optimization routine and diagram of the procedure can be found in supplementary materials, Tab. S2 and Fig. S4.

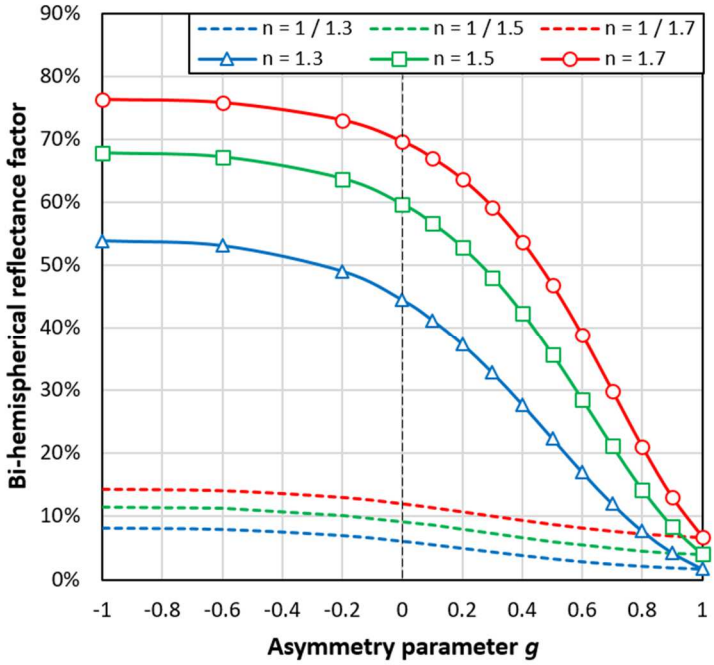

Figure 5: Bi-hemispherical reflectance of the diffuse flux as a function of the asymmetry parameter g of the Henyey-Greenstein phase function for a refractive index of the layer n=1.3, 1.5, or 1.7. Plotted for both cases: flux flowing outward (solid lines) and inward (dashed lines) the encapsulant sheet.

3.3 Model validation on known non-diffusing media: BK7 glass and EVA encapsulants

For the two following cases, as these encapsulants are not diffusing, the scattering parameters of the model are forced to 0 for the scattering coefficient s and to 1 for the asymmetry factor *g*. In this way, the model of this study is forced to use the same assumptions as the ones used for the determination of the optical constants of the BK7 glass and the EVA encapsulant (collimated beams only).

3.3.1 Comparison with literature for a BK7 reference glass

The model is applied on a 4.953 mm thick reference glass: the n-BK7 glass from SCHOTT. The refractive index n and absorption coefficient a of this material are well known (Schott Datasheets [43]). Extracted refractive index and extinction coefficient are plotted in Figure 6 : Absorption coefficient a (left) and refractive index n (right) of a SCHOTT glass n-BK7 obtained from the literature (black) and from the 4-flux model used in this study (blue). The agreement is very good between SCHOTT refractive index (which are values fitted with a Sellmeier model), and the raw value (wavelength by wavelength – no dispersion model) obtain with the 4-flux model of this study (Figure 6). SCHOTT gives the absorption coefficient data for only a few wavelengths. The two data sets are quasi-identical, except for one measuring point at 1500 nm. This difference is due to a change of detector in the integrating sphere that occurs at 1460 nm, and it is not significant: it produces a difference of less than 0.1% in transmission and reflection.

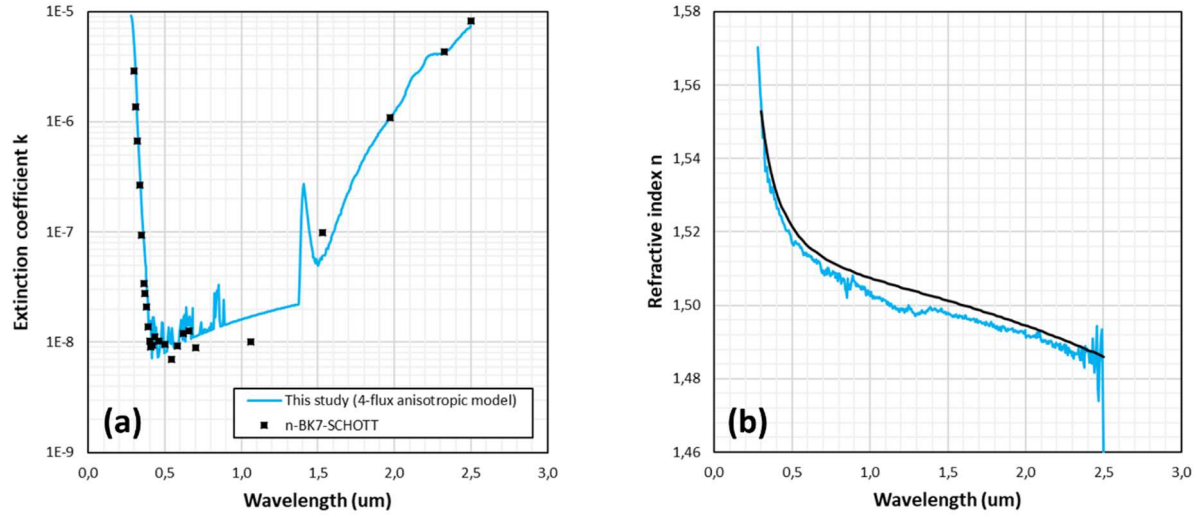

Figure 6 : Absorption coefficient α (a) and refractive index n (b) of a SCHOTT glass n-BK7 obtained from the literature (black) and from the 4-flux model used in this study (blue).

The experimental values of collimated-to-collimated and collimated-to-diffuse transmittances and reflectances are given on the Figure 7. The modelled values are also given on the figure, and are completely superimposed to the experimental values: the fitting error (RMSE) is smaller than 0.04 % for every wavelength. These results validate our approach, at least for the collimated 2-flux form, as the considered sample is very weakly scattering.

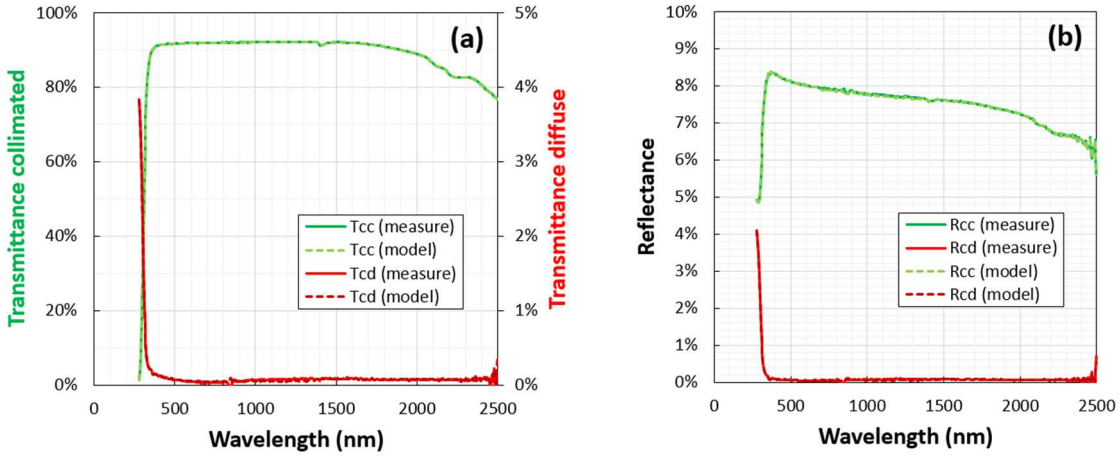

Figure 7: Comparison of experimental measurements of collimated-to-collimated (cc) and collimated-to-diffuse (cd) transmittances (T) on (a) and reflectances (R) on (b) with the values obtained with the model and extraction of optical constants after the fitting procedure for a SCHOTT glass n-BK7.

3.3.2 Comparison with literature for an EVA encapsulant

The model was also applied to a UV-transmissive encapsulant from the family of EVAs, which are known to be low-diffusing. The supplier is First Solar. The two samples are 387 and 598 µm thick. The values obtained are compared to the measurements published by Vogt *et al*. on a Bridgestone EVASKY S87 with 25 layers of EVA laminated together, to obtain more precision on the absorption coefficient [24]. The total thickness of the 25-layers sample is 10.2 mm, corresponding to a thickness of single layer of 400 µm. The results can be found in the Figure 8.

The results for the refractive index differ by less than 1 % in the visible range. This difference could be due to scattering from the surface state which lowers the reflectance of the collimated beam, or

by an interface consisting of an effective porous medium. This corresponds to a difference in the reflectance of 0.6 % absolute at an air/encapsulant interface. But this configuration never occurs in a real module: the encapsulant is always covered with glass. The reflectance coefficient at a glass/encapsulant is 0.001 % for a glass with refractive index of 1.5 and encapsulant with refractive index of 1.47. It becomes 0.01 % if the encapsulants has a refractive index of 1.47. Both reflectances can be considered as negligible.

The refractive index of the encapsulant also affects the optical coupling with the cell. The reflectance of a heterojunction cell encapsulated in an EVA with an index of 1.49 at 550 nm is 0.89 % (obtained with Sunsolve). If a material with an index of 1.47 at 550 nm is now used, the reflectance is 0.90 %. We can therefore conclude that the 1 % difference between the refractive index value obtained by Vogt *et al*. and obtained in this study has no impact either on the optical coupling between the encapsulant and the cell.

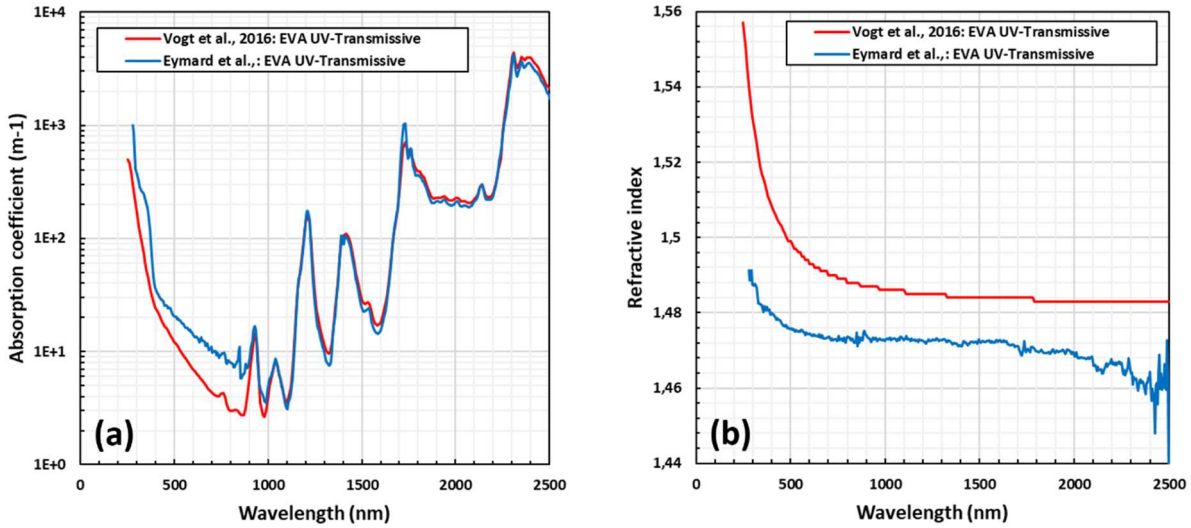

Figure 8 : (a) Absorption coefficient α and (b) refractive index n of a UV-Transmissive non-scattering glass n-BK7 obtained from the literature (red) and from the present 4-flux model (blue).

The absorption coefficient is similar throughout the 1000-2500 nm range: the absorption peaks are linked to the common bond C-H , C-O and N-H and their overtones [32]. Below 1000 nm, the difference is more pronounced, but it may be attributed to sample differences. Indeed, in this spectral range, the nature of additives may impact the absorption, and it is known that these additives and their proportions may differ among producers. In conclusion, even if minor differences have been observed, the absorption and refractive index on low diffusing EVA encapsulant have been found in good agreements with literature data.

4. Application of the 4-flux model on experiments and comparison with other approaches.

In this section, results obtained using the 4-flux model are discussed and compared to simplified approaches. Indeed, several other approaches, proposed for either fully transparent or highly scattering layers, allows the extraction of optical parameters. In the next section, these approaches are summarized, and benchmarked with the more general 4-flux approaches proposed in this paper in the following. Being more general, the same code used for 4-flux approaches can be tuned to this aim, after minor modifications detailed here after. Let's describe in the following approach 1 to 3, the fourth approach being the anisotropic four flux modelled previously described. The four approaches are compared for experimental measurements (Figure S5 - left) performed on two low UV-cutoff TPO samples of different thicknesses (0.667 mm & 1.141 mm), which can be seen in Figure S5.

4.1 Approach 1: Collimated 2-flux model applied on specular components of transmission and reflectance only.

The first approach is the standard procedure used for the extraction of optical constants of transparent materials using a spectrophotometer and neglecting light scattering. In this approach, the 4-flux model is reduced into a 2-flux model with only collimated components, and the absorption coefficient, as well as the refractive index n are extracted for any wavelength. Thus, this approach is a particular case of the more general 4-flux methods, and consequently the same code can operate it, provided that the scattering coefficient s is set to zero. Consequently, the optical thickness $o = (a + s)\ h$ reduces to a function of only the absorption a and thickness h of the sample: $o = ah$. The single scattering albedo ω is zero across the entire spectral range: $\omega = s/(a + s) = 0$. Since g is 1 and ω is 0, the tabulated average crossing parameter ϵ and forward scattering ratio ζ are unity, over the whole spectral domain considered. The reflectance of the collimated light is governed by the Fresnel angular reflectance. This model is applied to specular only experimental values of transmission and reflectance. Importantly, in this approach, the root-mean-square error RMSE function (that the extraction code tends to minimize) does not include experimental value of the diffuse transmittance and reflectance. Approach 1 can be considered as a "reference" approach.

4.2 Approach 2: Collimated 2-flux model applied on specular and diffuse components of transmission and reflectance

As seen previously, approach 1 performs an extraction of the optical parameters *n* and *a* from the specular measurements only. Simulated directional transmittance and reflectance may end up in good agreement with experiments, leading to low value of RMSE. However, as it ignores light scattering, the extracted value of optical parameters *n* and *a* are questionable. In other words, the values of RMSE only give an indication of the quality of the specular reflectance and transmittance curves fitting, but do not necessarily guarantee that the extracted parameters are correct. To better estimate the real value of the RMSE, this approach 2 is proposed. It uses the same extraction model than approach one (collimated flux only – no scattering) but apply it on the four experimental measurements (with diffuse reflectance and transmittance added) Thus, the calculation of the RMSE includes additional information on the experimental reality of diffusion phenomena in the material. Indeed, the error made by assuming that no light scattering occurs in the model (while it is not really the case in the experiment) is included in the calculation of RMSE. By this procedure, the comparison of the value of the RMSE calculated by approach 2 and the other approaches based on the 4-flux model that account for scattering (approach 3 and 4) is fairer. This approach can be considered as an adapted "reference" approach.

4.3 Approach 3: Collimated and isotropic diffuse 4-flux model applied on specular and diffuse components of transmission and reflectance

The third approach uses a 4-flux model: one collimated and one diffuse flux propagating forward, and one collimated and one diffuse flux propagating backward. The diffuse fluxes considered isotropic: diffusion is similar in all directions. This implies that the forward scattered part is the same as the backward scattered part. The asymmetry parameter of the Henyey-Greenstein phase function g is fixed to 0. Let's give details about the range of variation of the code parameters. First, the optimisation procedure is forced to look for refractive index n in the range 1.0 and 2.0. The optical thickness o is related to the absorption coefficient a, scattering coefficicent s and thickness h of the sample: $o = (a + s)\, h$. The single scattering albedo ω is free to vary between 0 and 1. Since g is 0 and ω and o are free to vary, the tabulated average crossing parameter ϵ can take values between 1 and 3 – around 2.5 where the absorption is negligible. The forward scattering ratio can take values between 0 and 1, and should be around 0.5 when the absorptance is negligible. The reflectance of the collimated light is governed by the Fresnel formula. The refection at interfaces of the diffuse light is computed as a function of n and g. This approach corresponds almost to the standard 4-flux model of Maheu *et al.*, 1984, where the forward scattering ratio is fixed to 0.5 and the average crossing parameter is 2.5.

4.4 Comparison of the four approaches root-mean-square error RMSE.

In this part, the four approaches are compared first in terms of their ability to reproduce the experimental measurements, i.e., in terms of the quality of the fit obtained, quantified by the value of the "root-mean-square error" RMSE equation (20) between the prediction and measurement. RMSE is a spectral value, as each wavelength is processed independently. Because of the normalization by the number of samples aforementioned, it is independent of the number of samples used for fitting. In our case, each experiment is performed on two samples of different thicknesses. RMSE values are plotted in Figure 9. Approaches 1 to 3 have been presented in the last section, while approach 4 corresponds to the 4-flux model proposed in this paper.

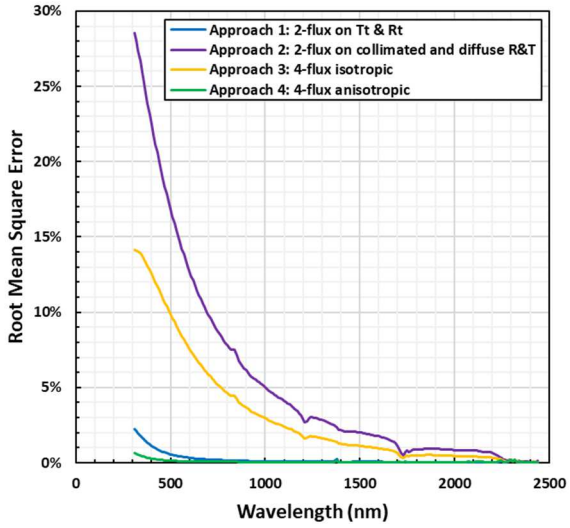

Approach	**1**	**2**	**3**	**4**
RMSE Integrated	0.20	5.38	3.08	0.08
Error $\boldsymbol{T_c}$	+0.33 -0.22	-0.10 +0.09	-0.19 -0.08	-0.09 +0.10
Error $\boldsymbol{R_c}$	-0.18 +0.30	-0.00 -0.04	-0.26 -0.27	+0.01 - 0.02
Error $\boldsymbol{T_d}$	+0.00 +0.00	+8.50 +12.26	+3.50 +5.08	+0.10 0.06
Error $\boldsymbol{R_d}$	+0.00 +0.00	+1.63 +2.32	-3.39 -5.03	+0.02 -0.01

Figure 9: **Left:** Root mean square error (RMSE) of the fitting procedure for each of the four approaches performed on two samples of low UV cut-off TPO family (thickness 667 µm and 1141 µm). **Right:** RMSE integrated on all wavelengths for each approach and details of error on each component for sample 1 (top value) and sample 2 (bottom value).

Experiments have been performed on samples of encapsulant from the low UV cut-off TPO family, chosen for its highly diffusing nature, recognizable at glance by its milky appearance. Experimental value of transmittances and reflectances are given in the supplementary materials, Fig. S5. Two samples of the same material but of different thickness are used, as this procedure allows to

minimize uncertainties. The first sample “TPO low UV cut-off 1” is obtained by laminating a simple sheet of encapsulant: its thickness (667 µm after lamination) is representative of the thickness that a real encapsulant would have in a PV module. The second sample “TPO low UV cut-off 2” is 1141 µm thick, obtained by laminating two sheets. The few unphysical experimental data where the absorption is found negative are simply removed to avoid any issue for the extraction procedure.

It can be observed that the four models follow a similar wavelength dependency: the error is higher in the ultraviolet range than in the infrared. This trend is like the one observed for the spectral dependency of the diffuse transmittance and diffuse reflectance curves. All models show a negligible error (< 0.2 %) beyond 2300 nm, where scattering is negligible. All these observations suggest that the fit error is mainly a consequence of the way scattering is treated.

At shorter wavelengths (300 nm), where the RMSE is the highest, approach 1 generates an error of 2.2 %, approach 2 an error of 28.5 %, approach 3 an error of 14 % and approach 4 an error of 0.6 %. As expected, the RMSE value with approach 2 is higher than the one with approach 1, as it includes in the error calculation the fact that diffuse reflectance and transmittance are ignored, in contrast with approach 1. Approach 3, an isotropic 4-flux model, gives better results than approach 2, but its overall error remains significant. Finally, approach 4, an anisotropic collimated/diffused 4-flux model, gives the best results, reducing the error by a factor of 20. Over the whole spectral range, the error of approach 4 is less than 0.6 %, which is an outstanding result. Indeed, even though the uncertainty of the spectrometer is estimated at 0.1 %, other uncertainties are added to the fit procedure. For instance, the tabulation of ϵ and ζ proposed by Rozé *et al.*, which is done by performing the fit of curves obtained by Monte-Carlo simulation, has an accuracy of 0.5 %. Moreover, the difference between a spectralon and a mirror as reference sample for reflectance can be as high as 0.6 % in the UV spectral range (supplementary materials, Figure S1). A closer look to the results obtained in term of absorption, refection index, scattering parameters and anisotropy are analysed in more details in the next section.

The table of Figure 9 summarizes the root mean square error, and the error on each component for sample 1 and sample 2. In this table, the values are not spectrally resolved, the mean of the error on the whole spectral range is computed instead. Using this procedure, results are easier to read, without significantly changing the overall conclusions. The details of spectral errors on each component can be found in supplementary materials, Fig. S6.

4.5 Comparison of the four approaches extracted optical parameters.

Regarding approach 1, the collimated transmittance is underestimated for sample 1 and overestimated for sample 2. The opposite is true for collimated reflectance. Ignoring light scattering, the model attributes the high reflectance values in the UVs to an artificially increase of the refractive index (Figure 10), resulting to unphysical values, higher than 2 (high-index polymer hardly exceed an index of 1.8 without the addition of nanoparticles [44]). This may also explain the decrease in transmittance over this spectral range for a single sample. However, as refraction is due to interfaces and not bulk, the impact of such a high value of the refractive index should be the same whatever the sample thickness. However, this is not the case: the total reflectance of sample 2 is higher in the UVs. The fit procedure therefore finds a compromise between the two values. As an indication, we can see that the difference between the total reflectance of sample 1 and sample 2 is 5.5 % at 300 nm, which corresponds approximately to a fitting error of 2.2 % for this wavelength.

Regarding approach 2, the model cannot explain the diffuse transmittance and diffuse reflectance, impacting the associated error. However, the fit obtained on collimated components is quite good: well below 0.5 % for transmittance and reflectance, for both samples. The low value of collimated transmittance and reflectance in the UVs region, in reality due to light scattering, are attributed within this model to absorption. Thus, in this model, the extracted absorption coefficient a corresponds more to an extinction coefficient $k = a + s$. Moreover, the extracted refractive index

n has a more plausible value in this approach: between 1.51 at 300 nm to 1.44 at 2400 nm. It can be fitted by a Sellmeier model.

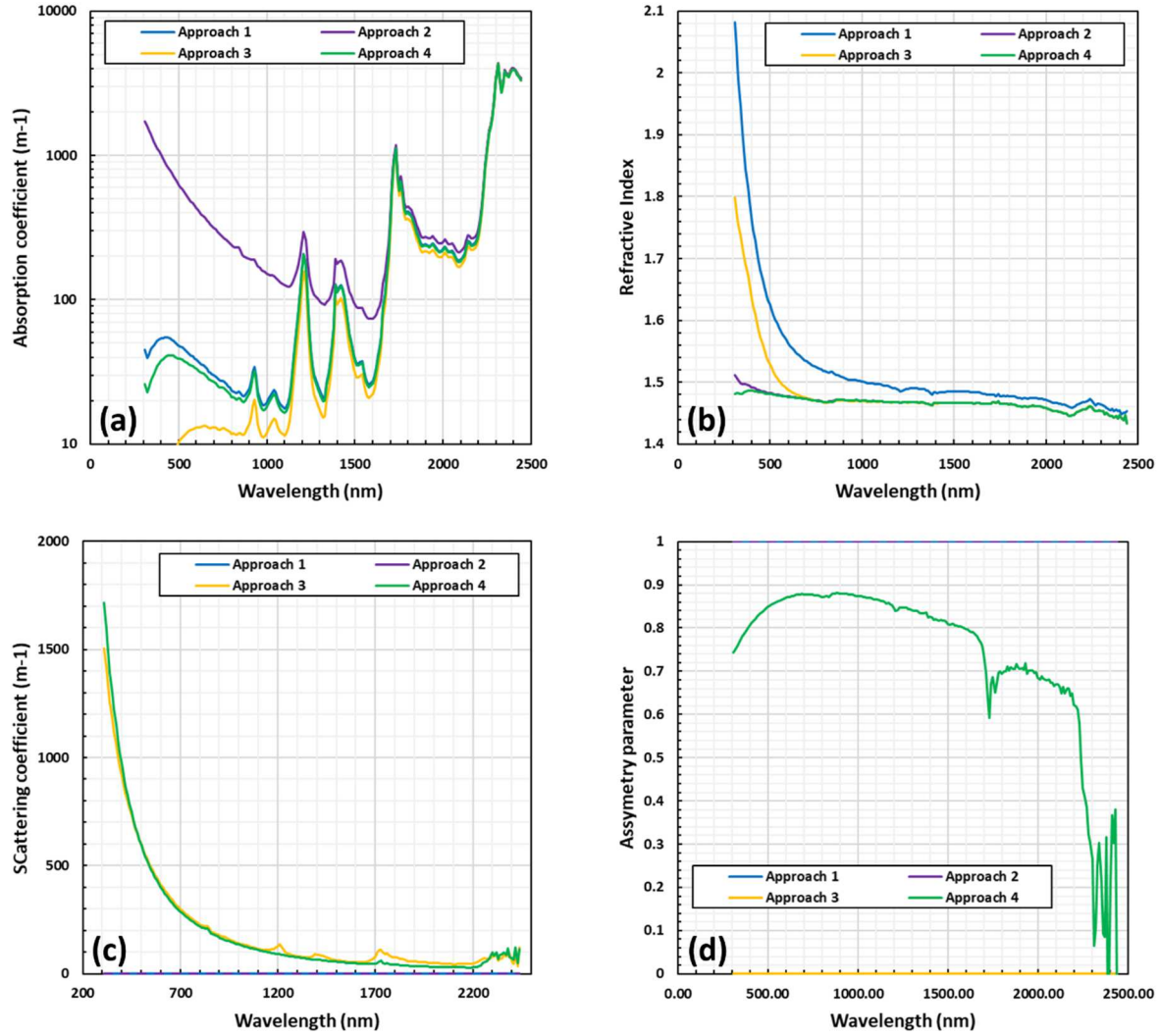

Figure 10: Results of the optimization applied to the two low UV-cutoff TPO samples of different thicknesses: absorption coefficient (a), refractive index (b), scattering coefficient (c) and asymmetry parameter (d), for approach 1 (blue), 2 (purple), 3 (yellow) and 4 (green).

Approach 3 overestimates the collimated transmittance by 1.5 % for sample 1 and 2 % for sample 2, and it underestimates the diffuse transmittance by 20 % for both samples. Collimated reflectance is also overestimated by more than 4.5 % for sample 1 and 4 % for sample 2, and diffuse reflectance is overestimated by 15 % for sample 1 and 20 % for sample 2. In this model, the scattering being isotropic, the proportion of light scattered backwards, and forwards, are the same. This is not what is observed: the diffuse transmittance is higher than the diffuse reflectance for both samples. In consequence, the model finds a compromise by overestimating one and underestimating the other. Moreover, at the interfaces, the diffuse reflectance coefficient between the encapsulant and air is very high, as expected for a Lambertian illumination. The reflectance coefficient increases with the angle of incidence. There is even a critical angle from which there is total internal reflectance. In this configuration, for a refractive index of 1.44, 55.8 % of the light is reflected. With a refractive index of 1.8, 73 % of the light is reflected. Due to the high internal reflectance, the effective path of the light in the encapsulant is higher than in the other model: the computed absorption coefficient needs to be smaller than in other model to explain the same total absorbance. The reason why the model

converges to high value of refractive index in the UVs region has not been found. The scattering coefficient s looks plausible.

Approach 4 is the best one in term of RMSE. The errors on each of the reflectance and transmittance components, are always less than 0.5 % for any wavelength with both samples. The trend of the optimized parameters is physically plausible: the asymmetry parameter *g*, in particular, takes values between 0.7 and 0.9 over the whole spectral range. In IRs, the scattering is low, so it can be assumed that the *g* values beyond 1500 nm are meaningless. However, the variation of *g* in the UVs and in the visible is necessary: if *g* is fixed at 0.8 over the whole spectral range, the RMSE in the UVs rises to 2 %, and the refractive index becomes high (1.7) for a polymer.

4.6 Impact of extracted optical parameters on the performance estimation of encapsulated silicon photo-voltaic module

Erroneous extracted optical parameters can significantly impact the performance estimation of encapsulated silicon photo-voltaic module: this part aims at estimating such errors due to volume light absorption and scattering only in the calculation of the short current circuit I_{sc}.

The performance of the reference, non-absorbing and non-diffusing encapsulated bulk heterojunction silicon PV module, has been done following the analytical model of Hanifi *et a*l. [45] : here, we consider the impact of low UV cut-off TPO encapsulant of thickness 667 µm under AM1.5 solar spectrum weighted by the external quantum efficiency (EQE) of an 21.78% HIT solar cell. This reference cell is described by the following parameters of the 2-diodes equivalent circuit: a saturation current J_{01} = 11.14 fA/cm², a recombination J_{02} = 6.871 nA/cm², a serie resistance Rs = 0.7 Ohm.cm², a photogenerated current J_{ph} of 37.65 mA/cm² and an infinite shunt resistance. Moreover, to simplify the discussion, only light absorption and backscattering (i. e. volume effects) have been considered, assuming that the refractive index is the same for all approaches. This is a substantial simplification, since for example in approach 1 and 3, the refractive index becomes much greater than 1.5 in UVs.

The results are summarized in the Table 1.

Effect on I_{sc}	**Approach 1**	**Approach 2**	**Approach 3**	**Approach 4**
Only absorption (%)	- 2.16 %	- 21.33 %	-0.79 %	-1.86 %
Only backscattering (%)	/	/	-10.10 %	-0.81 %
Remaining (%)	97.84 %	78.67 %	89.11 %	97.30 %

Table 1: Losses on photo-generated current due to absorption and backscattering for each of the four approaches. (Reference is a non-absorbing and non-diffusing encapsulated bulk heterojunction silicon PV module)

The most accurate approach (approach 4) predicts a loss on the I_{sc} by absorption of 1.86 % and a loss by backscattering of 0.81 %. In term of power conversion efficiency, this corresponds to -0.38 $\%_{abs}$ in efficiency of the module from absorption, and -0.17 $\%_{abs}$ from backscattering. Thus, the fact that the encapsulant diffuses light has a significant detrimental impact on the cell to module efficiency decrease, that should be considered when selecting encapsulant.

Moreover, it must be noted that the parameter extraction used also has a significant impact on the performance prediction. For instance, the isotropic scattering model tends to overestimate light back scattering (-10.1 % compared to -0.81 %) and specular models tend to overestimate absorption (-2.16 % for approach 1 and -21.33 % for approach 2).

5. An example of application of the 4-flux model: comparison of high and a low UV cut-off highly diffusive TPO optical properties

This part is devoted to the presentation of the results of two diffusive encapsulants of the TPO's family. The first one has been designed to absorb UVs (high UV cut-off) to prevent the module from degradation and ageing due to UV at the expense of module performance, while the second one lets them pass through (low UV cut-off). Although the exact composition of both materials has been kept secret by the manufacturer, the two material differs only by the presence of UV absorbers in the high cut-off TPO encapsulant. The nominal thickness of the two encapsulants, as claimed by the manufacturer, is 600 µm. The 4-flux model previously presented has been applied to both encapsulants, and the results are presented in the following.

5.1 Optical parameter extraction of high and a low UV cut-off highly diffusive TPO

The quality of the fit obtained for both encapsulants in term of "root-mean-square error" RMSE is shown in Figure 11. In the Visible-Infrared range, the error on both samples is similar, on average less than 0.1 %. In the visible range, the error increases as expected when the wavelength decreases, because light scattering becomes more and more important. For the high UV cut-off encapsulant, the error in the UVs drops to 0.1 % in the UV range, because the scattered flux is completely absorbed, while it remains high for the low UV cut-off encapsulant. For both samples the maximum error remains as low as 0.6 %, which is a satisfactory result.

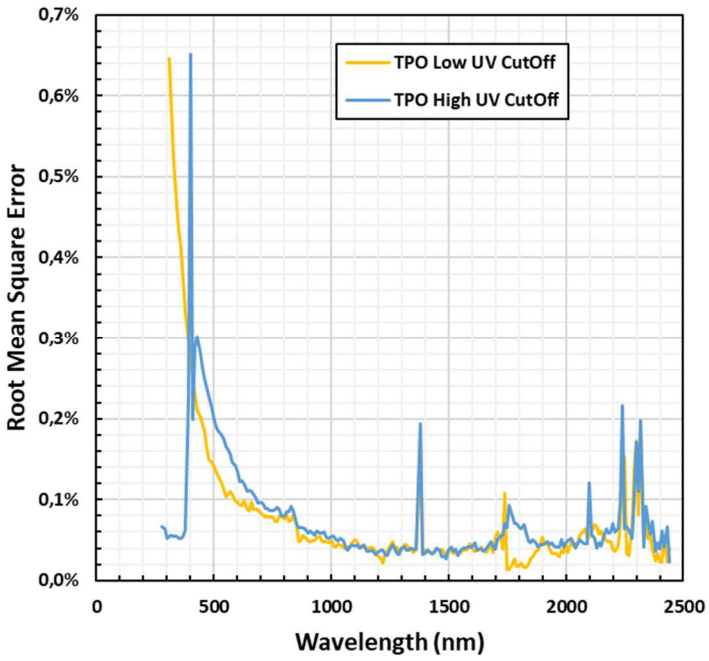

Figure 11: *Root mean square error obtained in the extraction of optical parameters using the 4-flux method for high and low UV cut-off TPO samples.*

Extracted optical parameters are given in Figure 12. The absorption coefficient α is found similar for the two samples from 450 to 2500nm, and significantly different in the UV range. This result is expected and shows that the extraction is reliable: different samples give identical results over the spectral range where their difference in chemical composition has no impact.

The results on the refractive index are also similar, it decreases from 1.49 in the UVs to 1.44 in the infrared at 2500 nm. A Sellmeier model, representative of transparent materials in the visible-infrared range, can satisfactorily model the spectral variation of the index. The local decrease present

at 2100 nm is probably a measurement artefact. Indeed, the refractive index is the real part of the complex index, and the absorption coefficient is related to the imaginary part. These two parts are linked by the Kramers-Kronig relations: a local variation of the optical index must be associated with a local variation of the coefficient, in a way that can be described by the Lorentz oscillator model. However, the absorption at 2100 nm is not the strongest of the spectral range, there is no reason it should cause a local variation of the index.

In both cases, the scattering coefficients show a similar variation in power law for both samples. It is more important for high-cut-off TPO, due to the presence of additional scattering particles (probably UV absorbers). Especially in UVs, it becomes ten times higher than for low cut-off TPO. Although it appears to be more diffusive, the diffusion lobe is slightly more specular for high cut-off TPO, as shown by the higher values of the g-asymmetry factor. However, the overall trend is similar for both samples: a more specular lobe in the UV-Visible (average g = 0.85) which becomes more and more isotropic in the infrared (g = 0.2 at 2400nm).

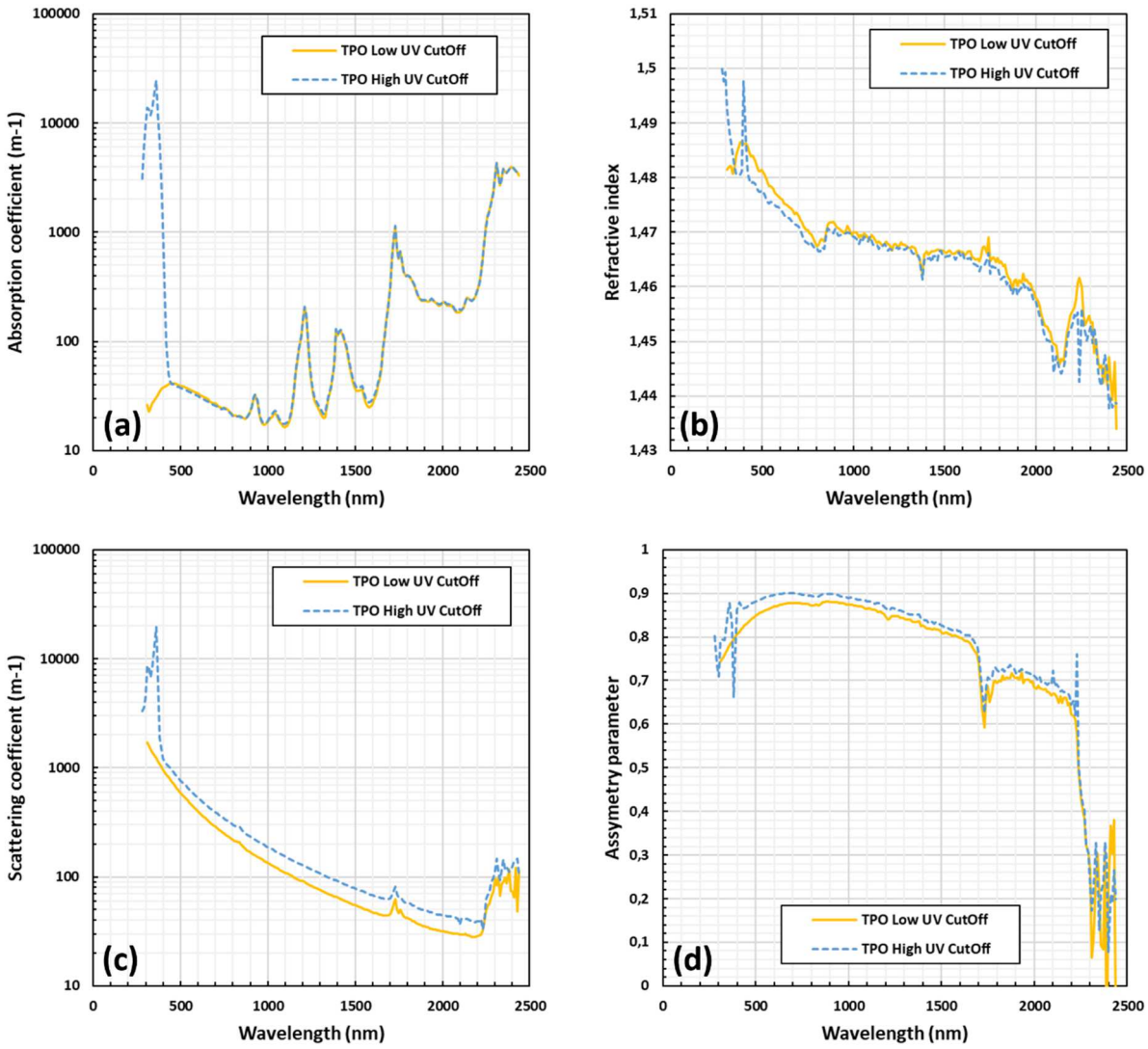

Figure 12: Optimization results of the optical constants of low (yellow) and high (blue dotted) UV cut-off TPO: absorption coefficient (a), refractive index (b), scattering coefficent (c) and asymmetry parameter (d).

5.2 *Impact of extracted optical parameters on the performance estimation of silicon photovoltaic module encapsulated by low and high UV cut off*

For the two 600 µm thick encapsulants, the effect on the photo-generated current is reported in the Table 2. The absorbed part represents a loss of 1.67 % in the approach of low cut-off TPO and rises to 3.81 % loss for low cut-off TPO: this represents an additional 2.1 % loss. The backscattered portion is about 0.7-0.8 % for both encapsulants, which is consistent with the values of nearly similar scattering coefficients.

Effect on I_{sc}	**TPO High UV Cut-off**	**TPO Low UV Cut-off**
Only absorption (%)	-3.81 %	-1.67 %
Only backscattering (%)	-0.77 %	-0.73 %
Remaining (%)	95.48 %	97.58 %

Table 2: Effect of optical constants on the photo-generated current (absorption and backscattering) for both sample of TPO (high and low UV cut-off).

Considering the reference cell described in the part 4.6, the absorbed part induces a loss of 0.86 $\%_{abs}$ for the low cut-off and 0.38 $\%_{abs}$ for the high cut-off TPO. The backscattered portion induces an identical loss of 0.17 $\%_{abs}$ for both samples.

In conclusion, the application of the 4-flux extraction model to two encapsulants of the same nature (TPO) but with a different behaviour in term of UVs absorption, appears consistent: similar values of optical constants (*a, s, n, g*) for wavelengths greater than 500 nm have been found. In the UV range however, the high cut off encapsulant has been found more absorbing, and a slight increase of the scattering coefficient, most likely due to the presence of UV absorbers, has been observed.

The higher absorption of high UV cut-off encapsulant results in 2.1 % higher photo-generated current losses I_{sc}. The scattering coefficients being similar, the associated losses due to backscattering on the I_{sc} are similar. For comparison, a UV-Transmissive EVA would cause an absorption loss of only 0.5 %. Characterized TPOs are therefore much more absorbent than EVA, and in addition generate backscattering.

6. Conclusion

Some of the new encapsulants used in PV modules are much more volume diffusive than the historical EVAs, such as the TPO and POE families. Characterisation of the optical constants of these materials is important for simulation (analytical model or ray-tracing), numerical prototyping and loss analysis of various PV module technologies. However, until now, light scattering effects in encapsulant volume were not properly included in the simulation of module performance losses.

This work shows that in order to correctly reproduce the measurements of spectral collimated and diffuse reflectances and transmittances a 4-flux model is required, combiningthehistorical model of Maheu *et al.*, 1984, and the tabulation of Rozé *et al.*, 2001. This later makes it possible to overcome the fit of the average crossing parameter and forward scattering ratio, the two parameters being expressed as a function of one, the asymmetry parameter of the Henyey-Greenstein phase function, reducing the number of extracted parameters.

Moreover, we have proposed an approximated procedure to calculate more precisely the bi-hemispherical reflectance coefficient of the diffuse flux accounting for anisotropy. Using this model, a numerical procedure of optimisation, based on the minimization of the root-mean-square error, has been implemented to extract the absorption coefficient *a* (m^{-1}, the scattering coefficient *s* (m^{-1}), the asymmetry factor *g* and the refractive index *n* from the measurement of the total transmittance T_t, the diffuse transmittance T_{cd}, the total reflectance R_t and the diffuse reflectance R_{cd}. This procedure combines experiments performed on two samples of different thickness for a better accuracy. The results obtained with this innovative approach have been compared with more conventional approaches, neglecting diffusion or assuming isotropic scattering, both on specular and diffusing encapsulants: it turns out that the improved 4-flux model is the best approach to reproduce accurately experimental data and obtained reasonable values of the optical parameters, and in particular the refractive index.

The proposed 4-flux model allows the accurate calculation of the absorption and backscattering that will take place in a module encapsulant, and the associated losses on photo generated current weighted by the EQE and the AM1.5 spectrum.. To the best of our knowledge, such backscatter loss has never been mentioned in cell to module analyses until now. As an example, results on two 600 µm thick TPO encapsulants (one high UV cut-off and the other low UV cut-off) show a backscatter loss of 0.75 % on average, and a loss on the I_{sc} by absorption of 1.67 % for the low cut-off against 3.81 % for the high cut-off.

Any study on module lifetime must take into account the evolution of optical parameters, not only silicon-based modules. The yellowing of some materials and the appearance of moisture ingress change the absorption and scattering of the material: the application of the presented method could be of great interest for durability studies. Also, in the future, this 4-flux model could be generalized to include emission terms and account for changes in wavelength, to deal with luminescent down shift encapsulants.

7. References

[1] VDMA, “International Technology RoadMap for Photovoltaic (ITRPV),” Tenth Edition, Mar. 2019.

[2] S. K. Chunduri and M. Schmela, “Advanced Solar Module Technology 2018 Report | TaiyangNews,” 2018. Accessed: Feb. 25, 2019. [Online]. Available: http://taiyangnews.info/reports/advanced-solar-module-technology-2018-report/

[3] I. Haedrich, U. Eitner, M. Wiese, and H. Wirth, “Unified methodology for determining CTM ratios: Systematic prediction of module power,” *Solar Energy Materials and Solar Cells*, vol. 131, pp. 14–23, Dec. 2014, doi: 10.1016/j.solmat.2014.06.025.

[4] U. Blieske and G. Stollwerck, “Glass and Other Encapsulation Materials,” in *Semiconductors and Semimetals*, vol. 89, Elsevier, 2013, pp. 199–258. doi: 10.1016/B978-0-12-381343-5.00004-5.

[5] A. Ganjoo, J. McCamy, A. Polcyn, Z. Ma, and P. A. Medwick, “Glass and Coatings on Glass for Solar Applications,” in *Springer Handbook of Glass*, J. D. Musgraves, J. Hu, and L. Calvez, Eds. Cham: Springer International Publishing, 2019, pp. 1635–1676. doi: 10.1007/978-3-319-93728-1_48.

[6] K. Burrows and V. Fthenakis, “Glass needs for a growing photovoltaics industry,” *Solar Energy Materials and Solar Cells*, vol. 132, pp. 455–459, Jan. 2015, doi: 10.1016/j.solmat.2014.09.028.

[7] M. R. Vogt *et al.*, “Measurement of the Optical Constants of Soda-Lime Glasses in Dependence of Iron Content and Modeling of Iron-Related Power Losses in Crystalline Si Solar Cell Modules,” *IEEE Journal of Photovoltaics*, vol. 6, no. 1, pp. 111–118, Jan. 2016, doi: 10.1109/JPHOTOV.2015.2498043.

[8] C. Rodríguez *et al.*, “Analysis And Performance Of Dispensed And Screen Printed Front Side Contacts At Cell And Module Level,” 2015, p. 8.

[9] Y. S. Khoo, F. Lu, T. M. Walsh, and A. G. Aberle, “Effective Finger Shading Width Of Screen-Printed Silicon Wafer Solar Cells In A Pv Module,” *27th European Photovoltaic Solar Energy Conference and Exhibition*, p. 3.

[10] M. Heinrich, A. Schmid, N. Mahmoud, M. Wiese, A. Grünzweig, and M. Mittag, “Analysis of Backsheet and Rear Cover Reflection Gains for Bifacial Solar Cells,” *33rd European Photovoltaic Solar Energy Conference and Exhibition*, pp. 18–22, Nov. 2017, doi: 10.4229/EUPVSEC20172017-1AO.2.3.

[11] K. R. McIntosh, N. E. Powell, A. W. Norris, J. N. Cotsell, and B. M. Ketola, “The effect of damp-heat and UV aging tests on the optical properties of silicone and EVA encapsulants,” *Progress in Photovoltaics: Research and Applications*, vol. 19, no. 3, pp. 294–300, May 2011, doi: 10.1002/pip.1025.

[12] L. Dunn, M. Gostein, and B. Stueve, “Literature review of the effects of UV exposure on PV modules,” in *NREL PV Module Reliability Workshop*, 2013, pp. 551–569.

[13] H. Holst *et al.*, “Application of a New Ray Tracing Framework to the Analysis of Extended Regions in Si Solar Cell Modules,” *Energy Procedia*, vol. 38, no. Supplement C, pp. 86–93, Jan. 2013, doi: 10.1016/j.egypro.2013.07.253.

[14] ISFH, *Daidalos*. [Online]. Available: https://www.daidalos-cloud.de/

[15] PVLightHouse, *SunSolve*. [Online]. Available: https://www.pvlighthouse.com.au/sunsolve

[16] N. Tucher *et al.*, “3D optical simulation formalism OPTOS for textured silicon solar cells,” *Opt. Express, OE*, vol. 23, no. 24, pp. A1720–A1734, Nov. 2015, doi: 10.1364/OE.23.0A1720.

[17] H.-Y. Li, L.-E. Perret-Aebi, R. Théron, C. Ballif, Y. Luo, and R. F. M. Lange, “Optical transmission as a fast and non-destructive tool for determination of ethylene-co-vinyl acetate curing state in photovoltaic modules: Optical transmission for determination of EVA curing state,” *Progress in Photovoltaics: Research and Applications*, vol. 21, no. 2, pp. 187–194, Mar. 2013, doi: 10.1002/pip.1175.

[18] M. C. C. de Oliveira, A. S. A. Diniz Cardoso, M. M. Viana, and V. de F. C. Lins, “The causes and effects of degradation of encapsulant ethylene vinyl acetate copolymer (EVA) in crystalline silicon photovoltaic modules: A review,” *Renewable and Sustainable Energy Reviews*, vol. 81, pp. 2299–2317, Jan. 2018, doi: 10.1016/j.rser.2017.06.039.

[19] G. Cattaneo *et al.*, “Lamination process and encapsulation materials for glass–glass PV module design,” *PV-tech*, p. 8, Mar. 2015.

[20] M. Kempe, “Encapsulant Materials for PV Modules,” in *Photovoltaic Solar Energy*, A. Reinders, P. Verlinden, W. van Sark, and A. Freundlich, Eds. Chichester, UK: John Wiley & Sons, Ltd, 2017, pp. 478–490. doi: 10.1002/9781118927496.ch43.

[21] H.-Y. Li, Y. Luo, C. Ballif, and L.-E. Perret-Aebi, “Effect of Cooling Press on the Optical Transmission Through Photovoltaic Encapsulants,” *Polymer-Plastics Technology and Engineering*, vol. 54, no. 4, pp. 416–424, Mar. 2015, doi: 10.1080/03602559.2014.958778.

[22] G. Ross and A. W. Birley, “Optical properties of polymeric materials and their measurement,” *Journal of Physics D: Applied Physics*, vol. 6, no. 7, pp. 795–808, May 1973, doi: 10.1088/0022-3727/6/7/203.

[23] R.-J. Zhou and T. Burkhart, “Optical properties of particle-filled polycarbonate, polystyrene, and poly(methyl methacrylate) composites,” *Journal of Applied Polymer Science*, vol. 115, no. 3, pp. 1866–1872, Feb. 2010, doi: 10.1002/app.31331.

[24] M. R. Vogt *et al.*, “Optical Constants of UV Transparent EVA and the Impact on the PV Module Output Power under Realistic Irradiation,” *Energy Procedia*, vol. 92, no. Supplement C, pp. 523–530, Aug. 2016, doi: 10.1016/j.egypro.2016.07.136.

[25] K. R. McIntosh, J. N. Cotsell, J. S. Cumpston, A. W. Norris, N. E. Powell, and B. M. Ketola, “An optical comparison of silicone and EVA encapsulants for conventional silicon PV modules: A ray-tracing study,” in *2009 34th IEEE Photovoltaic Specialists Conference (PVSC)*, Jun. 2009, pp. 000544–000549. doi: 10.1109/PVSC.2009.5411624.

[26] N. E. Powell, B. K. Hwang, A. W. Norris, B. M. Ketola, G. Beaucarne, and K. R. McIntosh, “Improved spectral response of silicone encapsulanted photovoltaic modules,” in *2010 35th IEEE Photovoltaic Specialists Conference*, Honolulu, HI, USA, Jun. 2010, pp. 002791–002794. doi: 10.1109/PVSC.2010.5616745.

[27] Y. S. Khoo, T. M. Walsh, F. Lu, and A. G. Aberle, “Method for quantifying optical parasitic absorptance loss of glass and encapsulant materials of silicon wafer based photovoltaic modules,” *Solar Energy Materials and Solar Cells*, vol. 102, no. Supplement C, pp. 153–158, Jul. 2012, doi: 10.1016/j.solmat.2012.03.008.

[28] G. M. Wallner, R. W. Lang, W. Platzer, and C. Teichert, “Optical properties of polymer films for transparent insulation,” *Macromolecular Symposia*, vol. 181, no. 1, pp. 399–410, May 2002, doi: 10.1002/1521-3900(200205)181:1<399::AID-MASY399>3.0.CO;2-O.

[29] G. M. Wallner, W. Platzer, and R. W. Lang, “Structure–property correlations of polymeric films for transparent insulation wall applications. Part 1: Solar optical properties,” *Solar Energy*, vol. 79, no. 6, pp. 583–592, Dec. 2005, doi: 10.1016/j.solener.2005.05.006.

[30] G. Oreski, D. Tscharnuter, and G. M. Wallner, “Determination of solar optical properties of transparent polymer films using UV/vis spectroscopy,” *Solar Energy Materials and Solar Cells*, vol. 94, no. 5, pp. 884–891, May 2010, doi: 10.1016/j.solmat.2010.01.012.
[31] M. D. Kempe, “Ultraviolet light test and evaluation methods for encapsulants of photovoltaic modules,” *Solar Energy Materials and Solar Cells*, vol. 94, no. 2, pp. 246–253, Feb. 2010, doi: 10.1016/j.solmat.2009.09.009.
[32] C. Pitois, A. Hult, and D. Wiesmann, “Absorption and scattering in low-loss polymer optical waveguides,” *Journal of the Optical Society of America B*, vol. 18, no. 7, p. 908, Jul. 2001, doi: 10.1364/JOSAB.18.000908.
[33] R. H. French, J. M. Rodríguez-Parada, M. K. Yang, R. A. Derryberry, and N. T. Pfeiffenberger, “Optical properties of polymeric materials for concentrator photovoltaic systems,” *Solar Energy Materials and Solar Cells*, vol. 95, no. 8, pp. 2077–2086, Aug. 2011, doi: 10.1016/j.solmat.2011.02.025.
[34] B. Maheu, J. N. Letoulouzan, and G. Gouesbet, “Four-flux models to solve the scattering transfer equation in terms of Lorenz-Mie parameters,” *Applied Optics*, vol. 23, no. 19, p. 3353, Oct. 1984, doi: 10.1364/AO.23.003353.
[35] S. Chandrasekhar, *Radiative transfer*. Courier Corporation, 2013.
[36] A. Ishimaru, *Wave propagation and scattering in random media*, vol. 2. Academic press New York, 1978.
[37] P. Kubelka and F. Munk, “An article on optics of paint layers,” *Z. Tech. Phys*, vol. 12, no. 593–601, pp. 259–274, 1931.
[38] B. Maheu and G. Gouesbet, “Four-flux models to solve the scattering transfer equation: special cases,” *Applied Optics*, vol. 25, no. 7, p. 1122, Apr. 1986, doi: 10.1364/AO.25.001122.
[39] W. E. Vargas, “Generalized four-flux radiative transfer model,” *Appl. Opt., AO*, vol. 37, no. 13, pp. 2615–2623, May 1998, doi: 10.1364/AO.37.002615.
[40] C. Roz, “Average crossing parameter and forward scattering ratio values in four-¯ux model for multiple scattering media,” *Optics Communications*, p. 13, 2001.
[41] J. Nocedal and S. Wright, *Numerical optimization*. Springer Science & Business Media, 2006.
[42] S. Q. Duntley, “The optical properties of diffusing materials,” *JOSA*, vol. 32, no. 2, pp. 61–70, 1942.
[43] Shott AG, “Schott Optical Glass Data Sheets,” Jan. 2017. [Online]. Available: https://refractiveindex.info/download/data/2017/schott_2017-01-20.pdf
[44] J. Liu and M. Ueda, “High refractive index polymers: fundamental research and practical applications,” *Journal of Materials Chemistry*, vol. 19, no. 47, pp. 8907–8919, 2009.
[45] H. Hanifi, C. Pfau, M. Turek, and J. Schneider, “A practical optical and electrical model to estimate the power losses and quantification of different heat sources in silicon based PV modules,” *Renewable Energy*, vol. 127, pp. 602–612, Nov. 2018, doi: 10.1016/j.renene.2018.04.060.